Materials Today Advances 17 (2023) 100352

Contents lists available at ScienceDirect

Materials Today Advances

journal homepage: www.journals.elsevier.com/materials-today-advances/

Programmable bio-ionic liquid functionalized hydrogels for *in situ* 3D bioprinting of electronics at the tissue interface

Vaishali Krishnadoss [a, b, 1], Baishali Kanjilal [a, c, 1], Arameh Masoumi [c], Aihik Banerjee [a], Iman Dehzangi [d], Arash Pezhouman [e], Reza Ardehali [e], Manuela Martins-Green [f], Jeroen Leijten [g], Iman Noshadi [a, *]

[a] Department of Bioengineering, University of California, Riverside, CA, 92521, USA
[b] Massachusetts Institute of Technology, Cambridge, MA, 02139, USA
[c] BICURE LLC, Yorba Linda, CA, 92887, USA
[d] Department of Computer Science, Rutgers University, NJ, USA
[e] Section of Cardiology, Department of Internal Medicine, Baylor College of Medicine, Houston, TX, USA
[f] Department of Molecular, Cell and Systems Biology, University of California, Riverside, CA, 92521, USA
[g] Developmental BioEngineering (DBE), Techmed Centre, University of Twente, 7522 NB, Enschede, Netherlands

ARTICLE INFO

Article history:
Received 6 November 2022
Received in revised form
21 January 2023
Accepted 24 January 2023
Available online 13 February 2023

Keywords:
In-situ 3D bioprinting
Bio-ionic liquid functionalization
Bioelectronics
Biomaterials
Biological tissue

ABSTRACT

The increased demand for personalized wearable and implantable medical devices has created the need for the generation of electronics that interface with living systems. Current bioelectronics has not fully resolved mismatches between biological systems and engineered circuits, resulting in tissue injury and pain. Thus, there is an unmet need to develop materials for the fabrication of wearable electronics that are biocompatible at the tissue interface. Here, we developed a tailorable gelatin-based bio-ink functionalized with a choline bio-ionic liquid (BIL) for *in situ* 3D bioprinting of bioelectronics at the tissue interface. The resultant photocrosslinked polymer is programmable, transparent, ion conductive, and flexible. BILs are stably conjugated with a gelatin methacryloyl (GelMA) hydrogel using photocrosslinking to make BioGel, which routes ionic current with high resolution and enables localized electrical stimulation delivery. Controllable crosslinking, achieved by varying reactants composition, allows the BioGel bio-ink platform for easy and rapid in-situ 3D bioprinting of complex designs directly on skin tissue. Bio-ionic modified polymers thus represent a versatile and wide-applicable bio-ink solution for personalized bioelectronics fabrication that minimizes tissue damage.

1. Introduction

Current advances in material science have resulted in the design and fabrication of biocompatible flexible electronic materials and devices used in wearable and implantable biomedical systems [1–6]. Such bioelectronic device designs often employ carbon-based materials, conductive polymers, and metals [2–6]. However, while most materials are cytocompatible and flexible, they often have limitations in mechanical and optical properties, such as poor stretchability or transparency, seen in high aspect ratio nanomaterials or specific conductive polymers, especially at the levels needed in specialized designs [3–8]. These limitations become critical in designing ultrathin or serpentine devices, curbing complexity, footprint, and overall device conductivity [3,8–12]. Additional limitations result from cytotoxicity and an inability to match the mechanics of human tissue [13–20].

Electronic conduction conferred by conductive biomaterials needs to be converted to ionic/electrolytic current at the electrode/electrolyte interfaces by electrochemical reactions to stimulate biological systems [10–14]. This requirement is critical to circumvent voltage drops over the interfaces higher than a specific limit (typically 1 V) which leads to pH changes, local heating, electrode degradation, and generation of highly reactive chemical species [4,11–17].

The increasing demand for rapid wearable and implantable biomedical devices has encouraged intraoperative approaches, such as *in situ* bioprinting, which enables the deposition of bio-inks

* Corresponding author.
E-mail address: inoshadi@ucr.edu (I. Noshadi).
[1] These authors have equal contribution.

https://doi.org/10.1016/j.mtadv.2023.100352

directly at the sites of injury to adapt to their specific structures and shapes [17,19–27]. Combining these approaches with freshly isolated cells from a patient could produce custom-made bioelectronics-based implants at the tissue interface [25,28–31]. Thus, the ability to generate novel biocompatible electronic device designs, which can interface with tissues and organs is indispensable [12–14,29–36]. The ionic conductivity, transparency, flexibility, and superior mechanical properties of biocompatible hydrogels, in addition to their proximity to those of natural tissue, and their ease of *in situ* 3D printability, make them potential candidates for such applications [14,36–40]. Furthermore, their ion transport aids the requirement of interfacial electron-to-ionic current conversion, ensuring superior safety in application [14–16]. An additional advantage of using ionic hydrogel conductors is the separation of electrodes from tissues, thus reducing the toxic tension created by chemical and electrochemical reactions [8,9,41–52]. The water content in these hydrogel structures also helps dissipate heat generated due to current passage, thus reducing the chances of burns and injuries in a wearable or implantable device [16,17,42,53–58]. While ionic hydrogels have been used to conduct electricity in electrochemical systems and connectors in circuits, existing material platforms are not stable in aqueous biological environments [16,17,58–64]. This instability occurs due to ion diffusion and low conductivity, severely limiting their applicability in integrated device designs for biological applications [19,65–70].

Choline-based bio-ionic liquids (BILs) are promising due to their biomimetic, immunomodulatory, and cytocompatible characteristics [16–19]. Previously, we showed that conjugation of BIL with biopolymers imparts conductivity to tissue scaffolds and synchronizes cardiomyocyte contraction [19–23]. In this paper, for the first time, a conductive, adhesive, and rheologically optimized transparent bio-ink platform for *in situ* 3D printing is introduced, which can be applied in tissue engineering and bioelectronics interface. A choline BIL is acrylated and photo-conjugated with a pre-functionalized gelatin methacrylate (GelMA) biopolymer to make BIL functionalized crosslinked hydrogel (BioGel), that can be used as a platform for easy, rapid, and direct *in situ* 3D bioprinting of complicated 3D designs at the interface of bioelectronics and biological tissue. The physical and electrical properties of the printed structure were characterized, and the cell-laden printed structures were found to be conductive and adherent to the epidermal layer of porcine skin. The tunability of BioGel properties can be achieved by varying the functionalization or the extent of crosslinking, thus providing a platform for generating versatile 3D printable structures that can be applied to integrated bioelectronics. The application of such systems is shown by creating light-emitting diode (LED)-based displays and skin-attached electronics and stimulators that provide localized current to *in vitro* (cell cultures) and *in vivo* (muscles) with reduced unfavorable effects. These electronic platforms may expand the application of bioelectronic-integrated tissue engineering in rapid drug prototyping, clinical translation, and regenerative medicine.

2. Materials and methods

Methacrylic anhydride and Gelatin (Type A) were purchased from Sigma-Aldrich. The photoinitiator, lithium phenyl-2,4,6-trimethylbenzoylphosphinate (LAP) was purchased from Allevi, Inc. Visible light that was used for crosslinking was attached to the Allevi 2 bioprinter. All chemicals were of analytical reagent grade and were used without further purification.

2.1. Synthesis of the bio-ionic ink

In this paper, we elaborate on a method to synthesize biocompatible BIL and conjugate it into a natural polymer, to yield an immunomodulatory conductive and adhesive bio-ionic ink (BI). Choline acrylate was synthesized by mixing choline bitartrate with acrylic acid at a 1:1 mol ratio as described previously by Noshadi et al. [19]. Briefly, the reaction was carried out at 50 °C for 5 h under an inert nitrogen atmosphere. It was then purified overnight by vacuum evaporation at room temperature. As a result, BIL was obtained and used for the next step. GelMA was synthesized using a method previously described in the literature [19]. Briefly, a 10 (w/v)% gelatin solution was methacrylated using 8 mL of methacrylic anhydride under inert conditions for 3 h. The resultant solution was purified by dialysis carried out for 5 days to remove unreacted methacrylic anhydride, and frozen at −80 °C for 24 h. The frozen acrylated polymer was lyophilized for 7 days. To form the BI, the acrylated polymer, GelMA, and BIL were added to distilled water at varying final polymer concentrations and mixed with the photo-initiator - 0.5 (w/v)% LAP [19]. The fabricated BI was photo-crosslinked in the presence of visible light in the Allevi 2 bioprinter at a wavelength of 450 nm and an intensity of 3 MW/cm^2 for 60 s. A commercially available handheld 3D bioprinter (Polyes Q1) was used for *in situ* 3D bioprinting of BI.

2.2. ^{1}H NMR and FTIR analyses of the bio-ionic ink

Proton nuclear magnetic resonance (^{1}H NMR) and Fourier-transform infrared (FTIR) spectroscopies were performed to characterize the BI. ^{1}H NMR was done by the standard dimethyl sulfoxide (DMSO) method using a Varian Inova-500 NMR spectrometer. ^{1}H NMR and FTIR (PerkinElmer Frontier™ FT-IR/FIR) spectra of choline bitartrate, choline acrylate, GelMA prepolymer, and BI were obtained.

2.3. Mechanical characterization of the bio-ionic ink

Mechanical testing of the BI was performed by using an EZ-SX Mechanical tester (Shimadzu). The elastic and compressive moduli were analyzed, and the mechanical test samples were prepared using fabricated polydimethylsiloxane (PDMS) molds. The test samples were immersed in Dulbecco's phosphate-buffered saline (DPBS) for 2 h at 37 °C prior to testing. The compression test was carried out by placing the samples between two compression plates and compressive stress at a rate of 1 mm/min was applied, thus recording the compression strain (mm) and compressive load (N) during each test. Similarly, for the tensile test, samples were held between tensile grips and stretched at a rate of 1 mm/min till the breaking point.

2.4. In vitro degradation and swelling studies on the bio-ionic ink

The BI was prepared for degradation tests as previously explained [19]. The test samples were lyophilized, weighed, and incubated in 1 mL of DPBS in a 24-well plate at 37 °C for two weeks. The buffer solutions were refreshed every three days to maintain constant activity. At prearranged time points, after 1, 7, and 14 days, the samples were removed from the solutions, lyophilized overnight, and weighed. The percentage of degradation (D%) of the samples was calculated in terms of the loss of weight. The equilibrium swelling ratio of the BI was estimated. For this purpose, cylinder-shaped hydrogels were prepared using a PDMS mold. The samples were washed thrice with DPBS. Then, they were lyophilized and weighed in dry conditions. After that, the samples were immersed in DPBS at 37 °C for 4, 8, and 24 h and weighed again after the immersion.

2.5. In vitro adhesive properties of bio-ionic ink

The shear strength of the BI was tested according to a modified American Society for Testing and Materials (ASTM) standard for tissue adhesives [16,21]. Two pieces of 2 × 2 cm were cut from a glass slide. To function as a base, a 1 × 1 cm layer of gelatin was coated onto each piece of the glass slide and dried overnight. The remaining uncoated area was covered with tape and the glass slides were clamped into the machine. A 15 μL drop of BI was crosslinked between the two layers of gelatin-coated glass slides. The two glass slides were clamped in the mechanical tester. A tensile load and a strain rate of 1 mm/min were applied. Shear strength was calculated at the point of detaching.

Wound closure was evaluated using the ASTM standard [21–23]. Porcine skin was obtained from a local store with excess fat removed and cut into 2 × 2 cm strips. Tissue samples were immersed in phosphate-buffered saline (PBS) before testing to prevent drying in the air. To simulate a wound, the tissue was then separated in the middle with a scalpel. 100 μL of the BI was placed onto the wound and crosslinked by visible light. The maximum adhesive strength for each sample was obtained at the tearing point.

Burst pressure was calculated by using the ASTM standard. A porcine heart was obtained from a local butcher. A 5 × 5 mm puncture was made in the left chamber of the heart and was placed in connection with a custom-built apparatus, which is made up of a syringe pressure setup, and a pressure meter, and air was flown using a syringe pump at 0.5 mL/s. The puncture made was sealed with a crosslinked BI before initiating the pump and sensor. Post rupture of the applied BI, airflow was terminated, and the pressure was measured.

2.6. 3D printing of the bio-ionic ink

The BI was prepared as mentioned before and was loaded into a 10 mL BD syringe with a 24-gauge blunt end needle. The pressure was varied to change the flow rate (7–15 kPa) of the BI and printed into different structures with a layer height of 0.1 mm. The prints were then crosslinked using the light in the printer for up to 1 min. STL files for lattice and multi-layered lattice were obtained from Allevi. For the support bath, Carbopol gel was prepared as described earlier [19,24]. Briefly, 1.8 (w/v)% of Carbopol ETD 2020 (Lubrizol) was dissolved in 50 mL of DPBS. 1.1 mL of 10 M NaOH was added to 50 mL Carbopol solution. Next, the Carbopol gel was centrifuged at 1000×*g* for 1 h until the gel became homogeneously dispersed.

2.7. In vitro biocompatibility study - cell proliferation, viability, and metabolic activity on the bio-ionic ink

On the surface of BI scaffolds 0.05 × 10^6 cells were seeded in 24-well plates with 500 μL of growth medium made of 10% fetal bovine serum supplemented Dulbecco's Modified Eagle Medium (DMEM). 2D cultures were maintained at 37 °C in a 5% CO_2 humidified atmosphere, for 7 days, and the culture medium was changed every 48 h.

The viability of the primary mouse myoblast C2C12 grown on the BI surface was evaluated by a commercial live/dead cell viability kit from Invitrogen. The instructions from the manufacturer were followed as protocol. The cells were stained with 0.5 μL/mL of calcein-AM and 2 μL/mL of ethidium homodimer-1 (EthD-1) in DPBS for 15 min at 37 °C. Fluorescent images were obtained on days 1, 4, and 7 after seeding using an Axio Observer Z1 inverted microscope (Zeiss). Viable cells and dead cells appeared green and red, respectively. Live and dead cells were quantified using the ImageJ software. The ratio of live cells to the total number of cells was determined as cell viability.

Cellular metabolic activity was evaluated on days 1, 4, and 7 post-seeding using the PrestoBlue assay (Life Technologies) as per the manufacturer's instructions. Briefly, cells were incubated with 10% PrestoBlue reagent for 2 h at 37 °C and the resultant fluorescence was measured (excitation 560 nm, emission 590 nm).

Cellular growth and proliferation on the BI surface were visualized using fluorescent staining of F-actin filaments and 4′,6-diamidino-2-phenylindole (DAPI) for cell nuclei. 2D cultures on days 1, 4, and 7 post-seeding were fixed with 4% paraformaldehyde. The samples were then incubated with Alexa-fluor 488-labeled phalloidin (1/40 dilution in 0.1% bovine serum albumin (BSA), Invitrogen) for 45 min. The samples were washed 3 times with DPBS and then counterstained with 1 μL/mL DAPI in DPBS for 5 min. Fluorescence imaging was done using an Axio Observer Z1 inverted microscope. The DAPI-stained nuclei were counted using the ImageJ software to quantify cellular proliferation.

2.8. In vitro biocompatibility study - cell proliferation and viability in 3D printed cell-laden bio-ionic ink

The BI was prepared as mentioned before and mixed with 0.7–1 × 10^6 of either C2C12 mouse myoblasts or human mesenchymal stem cells (hMSC) suspension. The cell laden-BI was then 3D printed on a petri-dish according to the aforementioned method, and the cell-encapsulated 3D printed constructs were then transferred to a 24-well plate with 500 μL of growth medium made of 10% fetal bovine serum supplemented DMEM. 3D printed cultures were maintained at 37 °C in a 5% CO_2 humidified atmosphere, for 7 days, and the culture medium was changed every 48 h.

The viability of the C2C12 or hMSC encapsulated in the 3D printed BI structure was evaluated by a commercial live/dead cell viability kit from Invitrogen. The instructions from the manufacturer were followed as protocol. The cells were stained with 0.5 μL/mL of calcein-AM and 2 μL/mL of ethidium homodimer-1 (EthD-1) in DPBS for 15 min at 37 °C. Fluorescent images were obtained on day 7 after seeding using an Axio Observer Z1 inverted microscope (Zeiss). Viable cells and dead cells appeared green and red, respectively.

Cellular proliferation inside the 3D printed BI construct was visualized using fluorescent staining of F-actin filaments and DAPI for cell nuclei. 3D printed cultures on day 7 post-seeding were fixed with 4% paraformaldehyde. The samples were then incubated with Alexa-fluor 488-labeled phalloidin (1/40 dilution in 0.1% BSA, Invitrogen) for 45 min. The samples were washed 3 times with DPBS and then counterstained with 1 μL/mL DAPI in DPBS for 5 min. Fluorescence imaging was done using an Axio Observer Z1 inverted microscope.

2.9. In vivo biocompatibility and degradation of the bio-ionic ink

Animal experiments were reviewed and approved by the Institutional Animal Care and Use Committee (IACUC), protocol 2018–004, at Rowan University. Experiments were performed as per relevant guidelines and regulations. Male Wistar rats (200–250 g) were obtained from Charles River (Boston, MA, USA). Anesthesia was induced by 4–5% isoflurane induction in an induction chamber, and the depth of anesthesia was assessed by the lack of pedal reflex to a toe pinch, followed by 2% or titrated isoflurane to effect maintenance dose delivered by a nose cone, followed by pre-emptive analgesia Meloxicam – SR (sustained release) administration 30 min before surgery. After inducing anesthesia, eight 1-cm incisions were made on the posterior

mediodorsal skin, and small lateral subcutaneous pockets were prepared by blunt dissection around the incisions. 2 × 2 mm disks of BI were implanted into the pockets. The anatomical wound was then closed, and the animals were allowed to recover from anesthesia. Animals were euthanized using anesthesia/exsanguination on days 4, 14, and 28 post-implantations. Finally, samples were retrieved with the associated tissue and placed in DPBS.

2.10. In vivo electrical stimulation of transverse abdominal (TA) muscle

The animal protocol was approved by the IACUC at Rowan University. The procedure was a non-survival surgery. Muscle stimulation of engineered hydrogels was evaluated *in vivo* after *in situ* 3D printing of BI in Male Wistar rats (weighing 200–250 g) according to previous studies [25]. The hind legs were shaved and prepped for surgery. The animal was placed in such a way that the TA muscle was exposed and a skin incision was made using a scalpel, then standard platinum electrodes with 10 mm separation (control) were used to electrically stimulate the muscle tissue. Two different voltages were applied: 0.9 V and 2.5 V. The actuation and height data were measured and collected using Keyence LJ-V700, for each voltage.

2.11. Histological analysis and immunofluorescent staining

The inflammatory response was characterized using histology on the explanted samples. The explanted samples were fixed in 4% paraformaldehyde for 4 h. Then the samples were incubated overnight at 4 °C in 30% sucrose. The samples were embedded in the Optimal Cutting Temperature compound (OCT) and flash-frozen in liquid nitrogen. Frozen samples were then sectioned using a Thermo Scientific CryoStar NX70 Cryostat.15-μm. The cryosections were mounted on positively charged slides. These slides were processed for hematoxylin and eosin (H&E) staining as per the manufacturer's instructions. Immunofluorescence staining was performed on the cryosections as previously reported [16]. The primary antibody used was Anti-CD68 (ab125212) (Abcam), and Alexa Fluor 594-conjugated secondary antibody (Invitrogen) was used for detection. All the sections were counterstained with DAPI (Invitrogen) and visualized on an Axio Observer Z1 inverted microscope (Zeiss).

3. Results and discussion

3.1. Synthesis and characterization of the BIL and the bio-ionic ink

The synthesis of BIL and BI is shown in Scheme 1. In order to integrate differing properties, the backbone of the polymer is conjugated with BIL. Choline, an acetylcholine precursor and methyl donor in lipid metabolism, is used as an ionic liquid. The ability of choline ionic liquid as a conductive and adhesive tissue scaffold was studied by Noshadi et al. [16,19]. Scheme 1a illustrates the chemistry of formation of the BIL through acrylation of choline bitartrate and scheme 1b shows the conjugation between GelMA and BIL to form the conductive and printable BI, and overall illustrates the one-step process of printing the bio-ink into a bioelectronic structure. BIL conjugation of the GelMA was carried out by mixing 7 (w/v)% GelMA with the BIL at a 0, 2 4, 6, and 8 (w/v)% concentration at room temperature to form the BI. The subsequent solution was photo cross-linked into the BI using LAP initiator and visible blue light for 60 s. The materials and methods section describes the process of making the BIL and its subsequent conjugation to the GelMA structure in detail. The synthesis of choline acrylate BIL from choline bitartrate was measured by FTIR and the conjugation of the BIL to the polymers was measured by ^{1}H NMR (Fig. S1).

The structural analysis of the reactions is shown in Fig. S1, where the ^{1}H NMR analysis of choline bitartrate, choline acrylate BIL, and BI7-4 (7% GelMA and 4% BIL) is shown that ascertains the conjugation of the BIL to the polymer (Fig. S1a). Methacrylate groups appeared in the conjugated polymer as characteristic peaks at ~5.7 ppm and ~6.1 ppm indicative of the conjugation of the polymer and ionic liquid leading to BIL incorporation in the polymer. The peak related to the hydrogen atom of acrylate at 5.9–6.3 ppm indicates the acrylation of choline bitartrate forming choline acrylate. In the FTIR spectra, the appearance of a peak at 1600 cm^{-1} indicates the formation of the ester bond via acrylation underscoring the formation of choline acrylate (Fig. S1b).

3.2. In vitro adhesive, physical, and mechanical properties of the bio-ionic ink

Hydrogels inherently have poor adhesion to biological tissues. Thus, its application as implants and bioelectronics is challenging and this limitation can be mitigated by surface modification. To address this, we designed a BI with high tissue adhesion brought about by physical and chemical interactions. The choline BIL functionalization also addresses hemostasis and tissue adhesion through interaction between the choline acrylate and the phosphatidylcholine on the cell membrane.

To study the capacity of the BI to perform as a firm adhesive scaffold, *in vitro* sealing properties of the BI x-y were evaluated with varying GelMA and BIL concentration levels, where the x and y indicate the GelMA and BIL concentrations in the reaction mixtures in (w/v)%, respectively. The polymer GelMA was used at x = 7, 10, 15 (w/v)% while the BIL concentration was kept at y = 0, 2, 4, 6 (w/v)%. Each composition was photo-crosslinked using 0.5 (w/v)% LAP as a photo-initiator. The primary impediments to successful tissue regeneration are oxidative stress and tissue damage [26]; these complications can be mitigated with BI as an alternative strategy, directly printable on the damaged sites. The *in vitro* response to shear and compressive stress, extension, tissue adhesion, and burst pressure were tested as per ASTM F2255-05. The samples were made with 7, 10, and 15 (w/v)% of GelMA due to the ease of printing. The shear strength of BI increases with rising BIL concentration, (Fig. 1a), following the same trend for all polymer concentrations. It is also interesting to note that the shear strength increased with increasing polymer concentration for the same level of BIL content. The shear strength of BI increased from 2.60 ± 0.20 kPa (7% GelMA with 0% BIL) to 32.13 ± 2.50 kPa for BI7-6.

The adhesive strength of the material was performed using a wound closure test. BI adhesive strength increased from 3.34 ± 1.35 kPa (7% GelMA with 0% BIL) to 34.3 ± 1.95 kPa for BI15-7 (Fig. 1b). The adhesive strength also increased slightly with increasing polymer concentration for the same BIL loading, although the trend is not monotonic. The burst pressure test establishes the ability of the bio-ink compositions to withstand fluid pressure from underlying tissues from within the damaged site. We tested burst pressure on the engineered BI, based on a variation of the ASTM F2392-04 standard testing. Burst pressure analyses of BI with 0% BIL were 1.89 ± 1.7 kPa and 4.95 ± 0.90 kPa for 7% GelMA and 15% GelMA, respectively (Fig. 1c). The burst pressures subsequently increased to 32.9 ± 1.1 kPa and 45.00 ± 3.00 kPa, for BI7-6 and BI15-6, respectively. Adhesive property is incumbent on electrostatic interactions and film-forming properties. Electrostatic interactions between polymer chains rise with increasing BIL loading which enhances the film-forming abilities [27,28]. With the increase in BIL concentration, the molecular weight per unit length of the polymer chain also increases due to a higher degree of

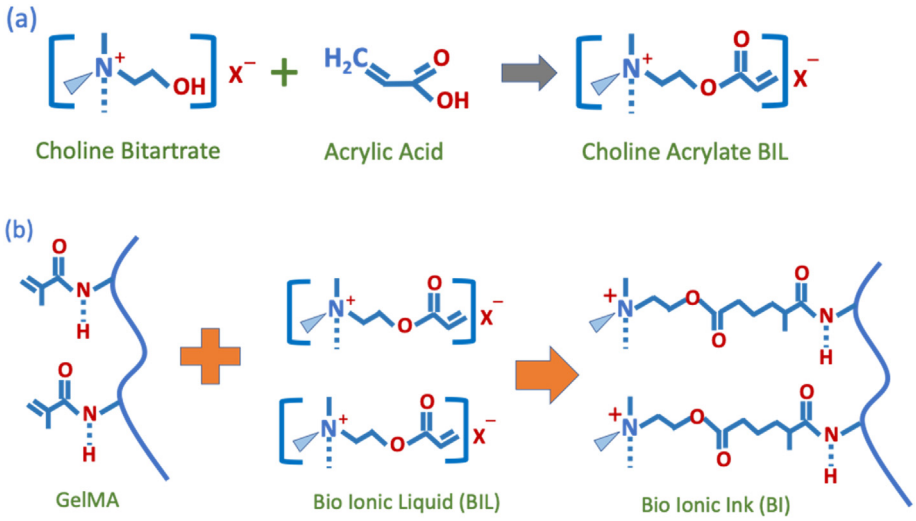

Scheme 1. Synthesis and fabrication of bio-ionic ink (BI). The panels show schematics for **(a)** the chemistry of formation of the BIL, and **(b)** the conjugation between GelMA and BIL to form the conductive and printable BI.

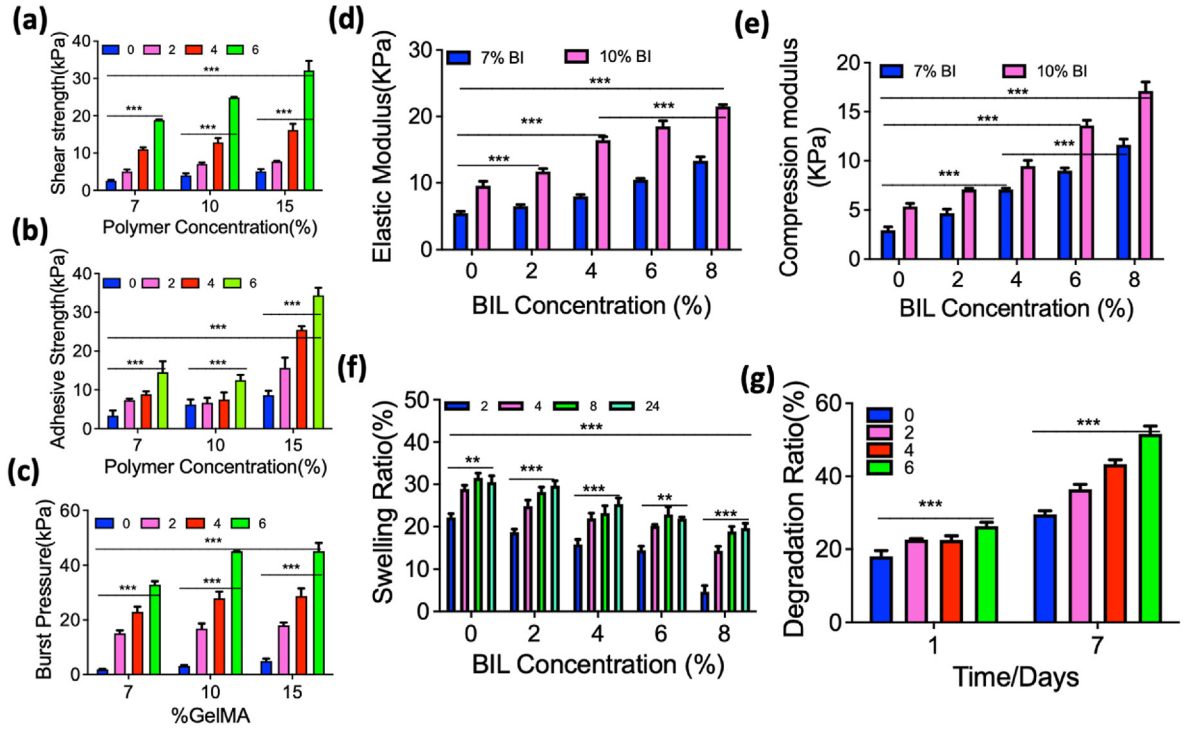

Fig. 1. *In vitro* sealing properties of the Bio-ionic Ink (BI) **(a)** Standard lap shear test to determine the shear strength **(c)** Standard wound closure test to determine the adhesive strength **(d)** Standard burst pressure test to determine the pressure ($n \geq 5$). Mechanical properties of BI: **(d)** elastic modulus and **(e)** compression modulus with GelMA (7, 10, 15 (w/v)%) and BIL concentration (0, 2, 4, 6 (w/v)%). Physical characterization of the BI - GelMA **(f)** swelling ratio and **(g)** degradation ratio with GelMA (7, 10, 15 (w/v)%) and BIL (0, 2, 4, 6 (w/v)%) concentrations with 0.5% lithium phenyl-2,4,6-trimethylbenzoylphosphinate (LAP) as the photoinitiator at 60 s visible light exposure. Data are means ± SD. P values were determined by one-way ANOVA (*P < 0.05, **P < 0.01, ***P < 0.001).

functionalization by bulky choline pendant groups. The BIL-based side groups significantly increase the strength of electrostatic interactions, preventing the chains from slipping against each other, and leading to high adhesive, shear, and burst pressure strength. While considering tissue surface adhesion, the choline groups from the BIL interact with the outer layer of phospholipidic bilayers of the exposed cell mass of tissues, forming a polar quadruple hence enhancing adhesion [29,31].

A degradable yet electroactive hydrogel with tunable physical and mechanical properties is vital for implantation. The swelling of BI determines the ability to withstand the water holding. The ink is composed of 7% GelMA with varying concentrations of BIL. The mechanical properties of the BI were characterized by tensile and compression tests to verify its capability to mimic the biomechanical features of the native extracellular matrix. Fig. 1d and e shows the elastic moduli and compression of the GelMA-BIL conjugated compositions synthesized using 7% and 10% GelMA with varying concentrations of BIL conjugation indicating that the elastic

and compression moduli of the BI are tailorable, modulated by varying the percentage concentration of GelMA and BIL. The mechanical strength was seen to increase with BIL concentration. With 0% BIL, the compression modulus was 2.93 ± 0.9 kPa with a tensile modulus of 5.4 ± 2.7 kPa. Interestingly, adding 6% BIL to GelMA significantly increased the compression and tensile moduli to 11.6 ± 5.8 kPa and 17.1 ± 0.9 kPa, respectively. These findings enable us to generate compositions with high elasticity and durability using a variable concentration of BIL as a fine-tuning property. BI compositions balance a delicate trade-off between structural integrity, flexibility, and resistance to shear, tension, or compression forces. This increase in compressive and tensile moduli with BIL functionalization is attributable to an increase in the intensity of electrostatic interactions. Tensile and compressive moduli also increase owing to an increase in the overall repeat unit and molecular weight with functionalization. The bulky choline BIL group functionalization makes the backbone stiff, making chain rotation increasingly difficult. Increasing BIL functionalization is directly correlated to an increase in polar and hydrogen bonding. These strong interactions impede the uncoiling and slippage of chains with the BIL group acting as a physical crosslink, tightly tethering the structure together.

The swelling was determined after 2-, 4-, 8-, and 24-h as shown in Fig. 1f. GelMA without BIL functionalization swelled up faster and to a greater extent than other compositions, reaching a maximum swelling of 34%. For the polymers functionalized with 2%, 4%, 6%, and 8% BIL, the initial water uptake and swelling are gradual, followed by a rapid increase as time passes. With increasing levels of BIL functionalization, the final swelling levels achieved were lower. As polymer chains absorb water, they form overlapping hydrated regions, the size of which is dictated by the concentration of BIL functionalization. With 0% BIL functionalization, the intrinsically hydrophilic polymer slowly opens allowing water in, till the crosslinks prevent any further structural expansion and swelling. BIL functionalization enhances the interaction between polymer segments causing them to tether strongly to each other via electrostatic interactions which act as physical “cross-links”, causing an initial resistance to hydration. The rate of hydration thus decreases with increasing BIL functionalization. For polymers, the density of crosslinking determines final swelling, hence limiting the extent to which the polymers can swell [36].

Similarly, *in vitro* degradation tests can be a good indicator of *in vivo* performance under physiological conditions [37]. The degradation behavior of the BI compositions is shown in Fig. 1g. The degradation percentage increases with BIL concentration. The degradation of the material with 0% BIL functionalization increases from 19% (day 1) to 32% (day 7) and, the degradation of the BI with 6% BIL functionalization increases from 27% (day 1) to 44% (day 7). The quaternary ammonium head in the choline BIL pendant group conceivably acts as a hydrolysis catalyst to facilitate hydrolysis of the integrated functionalities in the polymer backbone causing its degradation.

3.3. In vitro conductivity and transparency of the bio-ionic ink

Electrochemical characterization of the BI using electrochemical impedance spectroscopic frequency response Nyquist plots with glassy carbon electrode, at 0.1 V was done (Fig. 2a, b, and c). Higher frequency input is represented by the left-hand side of the curves. In impedance spectroscopy, the sample is considered as a parallel plate capacitor, which forms a double-layer capacitance electrode, with a representative circuit comprising of film resistances and capacitances in parallel, connected to a double-layer capacitance in series. The total impedance is incumbent on local motion and oscillation of the charged BIL pendant groups. It is primarily represented by the distorted circular portion of the graph [32]. The straight line in the Nyquist curves represents electric relaxation at low frequencies and is related physically to the diffusion of the solvent imbued in the polymeric gel matrix and portends to the alignment of BIL groups, molecular migration, distortion of polymer chains, molecular vibration, and solvent convection. These are contributors to thermodynamic hysteresis leading to energy dissipation. The linearity of the plots in the low-frequency areas indicates that the BI behaves like a resistor at low frequencies. As the frequency increases, its behavior converts like a resistance-capacitance transmission line circuit [33–35]. Conductivity was measured using the three-electrode system for BI samples, and the results are shown in Fig. 2d. Control samples made with 7% GelMA and 0% BIL functionalization had a conductivity of 9×10^{-3} S/cm, while 15% GelMA with 0% BIL functionalization showed a conductivity of 6×10^{-3} S/cm.

With the introduction of BIL functionalization, the conductivity was seen to increase to 13.2×10^{-2} S/cm for BI7-6 and to 27×10^{-2} S/cm for BI15-6, as shown in Fig. 2d. Fig. 2e shows a microscope slide coated with the electrolyte and GelMA. Higher levels of BIL functionalization may polarize the polymer chains, causing the movement of chain segments. Every BIL pendant group is accompanied by a free and mobile counter-ion. Thus, with high levels of BIL functionalization, there is a higher concentration of mobile counter-ions and hence higher conductivity, which also results in greater polarization of the solvent molecules thus contributing to a further increase in conductivity.

To study the transparency of the BI in comparison to commercially available electrolytes, both the electrolyte and the BI were coated on a glass slide. When illuminated with visible light the carbon nanotubes (CNT) and 1-Ethyl-3-methylimidazolium - tetrafluoroborate ($EMIBF_4$) electrolytes are opaque (Fig. 2f–h). Improved optical transparency of the hydrogel along with the conductivity of the BI proffers a favorable material for various bioelectronic applications. Especially, hydrogels used in electronics and biological interfaces are required to be conductive, highly adhesive, stretchable, and transparent for the unified integration of electrophysiological recordings and other applications.

3.4. In vitro biocompatibility of the bio-ionic ink

To investigate biocompatibility, *in vitro* commercial live/dead assay was used. The assay determined the viability of C2C12 cells growing on the surface of BI over 7 days. F-actin/DAPI immunofluorescent staining was used for studying cell attachment and spreading on hydrogels. The results show a 99% viability of seeded cells on day 7. Furthermore, the metabolic activity of the primary cultures quantified by the Presto Blue assay was shown to increase significantly throughout the duration of the culture. These results underscore that the BI has the potential for application as a biocompatible ink.

Fig. S2a-g shows the *in vitro* biocompatibility of BI7-4. The representative F-Actin/DAPI fluorescent images are shown in Fig. S2a, c. Cells cultured on top of the BI layer, stained with Phalloidin and DAPI, show enhanced cell proliferation with a visible increase in both the actin-cell membranes (green) and DAPI- cell nuclei (blue). The Live/Dead images on days 1, 4, and 7 post-seeding of C2C12 are shown in Fig. S2b, d as cell cultures with the live cells being represented by green and dead cells by red fluorescence demonstrating an increase in the density of live cells and very little change in the density of dead cells.

We next performed quantification of cell proliferation, viability, and metabolic activity based on the number of DAPI-stained cell nuclei, percentage viability of live/dead images, and relative fluorescence units (RFU), using Presto-Blue assay respectively

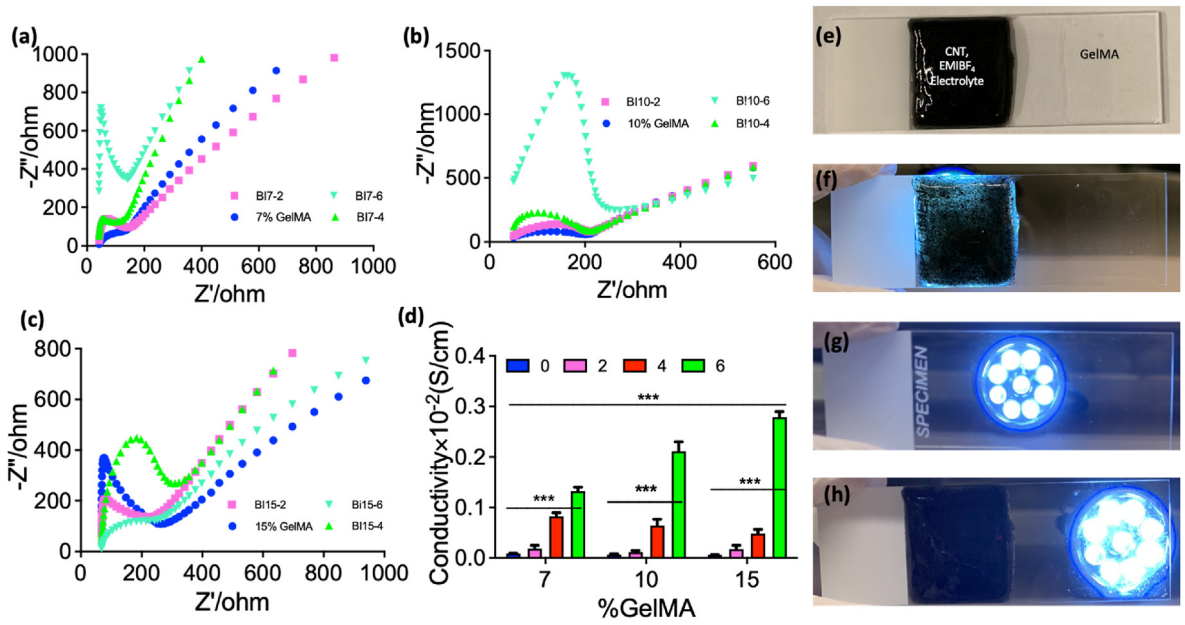

Fig. 2. Conductivity of the bio-ionic ink (BI). Nyquist plot ($n \geq 5$) with **(a)** 7% GelMA **(b)** 10% GelMA **(c)** 15% GelMA with varying percentages of BIL (0–6 (w/v)%) to form various percentages of the BI. **(d)** Quantitative evaluation of the Nyquist plot to represent conductivity value in S/cm. Comparison of the optical transparency of BI7-4, GelMA, and electrolyte made up of CNT, PVDF, and $EMIBF_4$ used as conductive materials in various applications **(e)** Microscope slide coated with the electrolyte and GelMA. Evaluation of the optical transparency of material by passing light through **(f)** CNT electrolyte, **(g)** uncoated slide, and **(h)** GelMA. Data are means ± SD. P values were determined by one-way ANOVA (*P < 0.05, **P < 0.01, ***P < 0.001).

(Figs. S2e–g). Both the control experiment and the BI composition matrix showed a significant increase in live cells indicating significant cell viability and cytocompatibility, with little to no difference compared to the control. Biopolymers degrade via hydrolysis in aqueous media and buffers to yield oligomers, monomers, and smaller moieties. Despite thermodynamic favorability, the degradation rate is incumbent and reduced by folding and assembly [38]. Given the imminent degradation of biopolymers, implant structures should be critically designed by the incorporation of structural moieties which will metabolize into non-toxic byproducts. A case in point is poly (β-amino ester) (PBAE), a gene delivery polymer, which upon degradation, causes little cytotoxicity due to benign products of hydrolysis [39].

The cytotoxic mechanism consists of necrosis, damage to cell membranes and organelles as well as apoptosis [40,41]. Polycations are also thought to induce phospholipid hydrolysis causing elastic stress on the membrane by interaction with the cell membrane creating an inversion in the lipid bilayer causing phase separation of lyso-phospholipids [42–44]. Cell membrane lysis is influenced by the molecular weight of the polycation. Cytotoxicity is thus incumbent on a tradeoff between membrane hydrolysis and the intrinsic cellular repair system. If the repair can counterbalance membrane lysis, the material remains cytocompatible, with mitochondrial activity powering the repair [45]. Biocompatibility is influenced by the molecular weight, and charge density of polymer chains [46]. Higher charge density causes greater cellular transfection and higher cytotoxicity. Rigid polymers interact less with cell membranes causing lower cytotoxicity [47–49]. Often, cytotoxicity is directly correlated to the presence of high cationic charge density and polymer chain flexibility [50]. In the GelMA and BioGel conjugate BI structure, the charge density due to BIL conjugation has been kept at low levels. The gelatin backbone in GelMA, and the methacrylate-coupled choline moiety, also limit conformational flexibility to prevent excess transfection type interactions. This conformational flexibility limitation is augmented by a light cross-linking to form a network, which balances out mechanical strength with an adequate increase in chain conformational rigidity due to reduced degrees of freedom, offering an advantage in enabling low cytotoxicity [51,52].

3.5. 3D printing of scaffolds from the bio-ionic ink and evaluation of the biocompatibility of the printed scaffolds

3D printing of C2C12 cell-laden constructs using BI7-4 is shown in Fig. 3. A digital image of printing BI using the Allevi 2 printer is shown in Fig. 3a. The BI7-4 can be easily printed into any shape or lettering permitting fine details. The Live/Dead staining of C2C12 cells encapsulated in the 3D printed structure is shown in Fig. 3b and c. The cells were encapsulated in GelMA and visualized in 3D, with living cells depicted in green, and dead cells in red fluorescence. To visualize the cell proliferation F-actin (green)/DAPI(blue) staining of the cells encapsulated in the 3D printed structure is shown in Fig. 3d and e. Fig. 3n compares the aspect ratio of the cells printed and cultured in 2D, the aspect ratio is the ratio of the total length to average breadth. In a 2-D culture, the cells are scattered on top of each other and randomly oriented. When they are encapsulated and 3D printed, the cells align, and that can be an advantageous feature depending on the intended application.

Biocompatibility and cell viability comparison between scaffolds printed using 7% GelMA and BI7-4 and hMSC, which are more sensitive to culture conditions than C2C12, are shown in Fig. 3f–k, respectively after 7 days in culture. In this 3D visualization, the BI with 4% BIL conjugation is shown to be as good as unfunctionalized GelMA for cell viability and adhesion, underscoring the absence of any adverse effect of the BIL conjugation. Cell adhesion to various conducting polymers has been known to be electrically controllable, especially where there are biomolecules that may be differentially oriented or diffused. Electrical control is achieved upon the accessibility of surface ligands to cellular receptors or general protein recognition [53–55]. The proteins and integrins responsible for the cellular adhesion to a matrix are held to the cellular cytoskeleton by a focal adhesion (FA) complex. Force transmission to

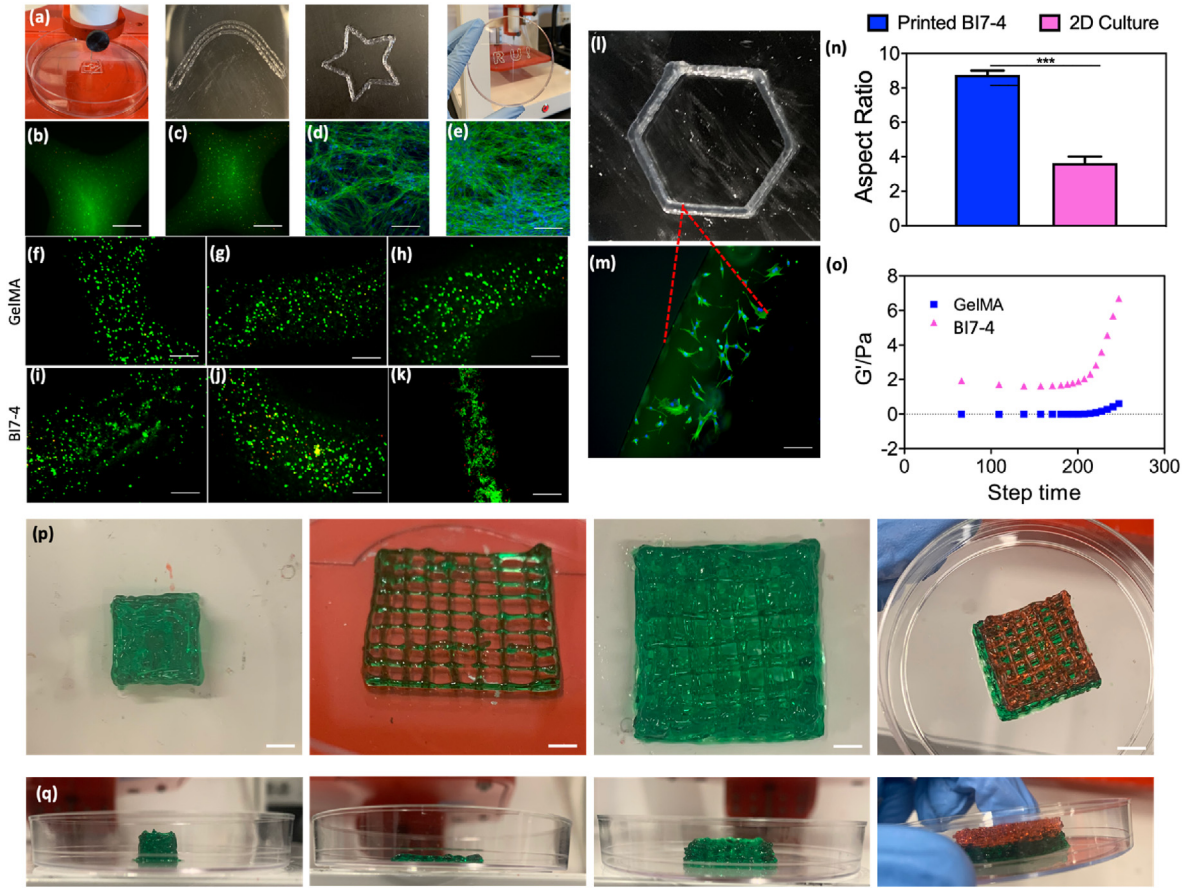

Fig. 3. 3D printing of cell-laden constructs using BI7-4 **(a)** Digital image of printing bio-ionic ink (BI) using Allevi 2 printer. **(b, c)** Live/Dead (green/red, respectively) and **(d, e)** Actin/DAPI (green/blue) staining of C2C12 cells encapsulated in the 3D printed structure. Live/Dead staining of hMSC and comparison between scaffolds printed using **(f–h)** 7% GelMA, and **(i–k)** BI7-4, after culturing for 7 days. **(l)** Digital image and **(m)** Actin/DAPI staining of printed hMSC encapsulated in BI **(n)** Comparison of the aspect ratio of the hMSC 3D printed and cultured in 2D. Data are means ± SD. **(o)** Rheology of GelMA and BI7-4 with 0.5% LAP as a photoinitiator at 60 s visible light exposure. **(p, q)** Digital image of printing of solid block, 2,4, and multi-layer lattice BI using Allevi 2 printer. P values were determined by Student's t-test (*P < 0.05, **P < 0.01, ***P < 0.001) (scale bar = 1 mm). (For interpretation of the references to color in this Figure legend, the reader is referred to the Web version of this article.)

the cellular cytoskeleton occurs via the FA proteins connecting the integrins to cellular actin filaments forming an adhesion complex. FA formation is critical to cell signaling, migration, proliferation, and differentiation and hence of utmost importance for tissue engineering applications [56–58].

The BioGel-based BI composition is capable of showing ion conductivity and a capacitive ability due to the BIL functionalization, which maintains its conductive advantage as a matrix while allowing cellular adhesion and proliferation.

Fig. 3o shows the rheology of GelMA and BI7-4 with 0.5% LAP as a photoinitiator at 60 s visible light exposure. Since the BI is photo-crosslinked, a quasi-solid state viscoelastic behavior is expected, which is represented by the storage modulus (G′) and loss modulus (G″), with the former representing the solid-state behavior of the sample while the latter representing the liquid-state part of the sample occurring from internal friction while the material flows. A large storage modulus leads to hysteresis losses in the form of heat dissipation during the shear-deforming 3D printing process, especially with cells included. The heat dissipation works to the imminent disadvantage of the sample in the given tissue engineering application as it may adversely interact with cellular proteins deforming them and impeding cellular adhesion and proliferation [59]. On the other hand, the elastic portion remains stored in the deformed material as potential energy, arising from stretching the internal substructures, that may be achieved without bond breakage and works to impart resilience [60].

The storage modulus was seen for both the control unfunctionalized GelMA and the BI7-4 to rise with an increase in step time. However, the increase in the case of the BI composition is much more rapid beyond a step-time input of about 250, which may be attributed to structure formation owing to much higher inter and intramolecular electrostatic interactions acting as “physical cross-links” at a more rapid pace of deformation. At a lower deformation rate, time is accorded to the sample to flow and hence the absence of structure formation, rigidity, and a high storage modulus at low deformation rates. It also shows the variation of the loss modulus with the deformation rate. Tan delta, the ratio of the loss modulus to storage modulus is much lower than 1, indicating the predominantly elastic nature of the cross-linked polymers, which works to advantage in tissue engineering, especially those involved in dynamic environments.

To show the printing fidelity, lattice constructs were printed up to 16 layers by optimizing the speed and pressure, as shown in Fig. 3p and q. The 16-layer 3D printing of BI was achieved using a Carbopol support bath, providing structural integrity to the printed constructs. As anticipated, the printed construct was stable after the cross-linking. GelMA and BIL composition forms BI, a conductive and adhesive hydrogel matrix, and is 3D printed using an

extrusion-based Allevi bioprinter. After printing, the structures were measured for conductivity, acquiring the cell-laden hydrogel structures via encapsulation of the hMSC. The orientation and shapes of the biostructure can be varied based on the composition of the polymer, BIL, air pressure, and other parameters in the printer and thus can be manipulated for any application necessary. To use the BI as an adhesive and conductive patch in *in vivo* applications, the interaction between the BI and tissue is vital. Despite the availability of commercial wearable epidermal bioelectronic devices, there is a need for a transparent, soft, and flexible material that is on par with the epidermal layer of the skin [61].

3.6. *In vivo* biocompatibility and degradation of the bio-ionic ink

In vivo degradation of the BI was evaluated by subcutaneous implantation into rats. Samples explanted on days 4, 14, and 28 were used to study compatibility and degradation. *In vivo* degradation and changes in tissue morphology were characterized by Hematoxylin and Eosin (H&E) staining. The staining results indicate the presence of hydrogel until day 4. The tissue architecture showed no significant inflammatory response implying that the BI may not have caused any adverse inflammatory responses. Fluorescent immunohistochemical staining for CD68 macrophages was used to characterize local immune response. CD68 macrophage invasion at the adhesive-subcutaneous tissue interface was seen on day 4 but was absent after 28 days. Fig. 4a–d shows the *in vivo* biocompatibility of GelMA and BI7-4. Fig. 4a–d show the representative H&E staining and fluorescent immunohistochemical analysis, respectively. The presence of macrophages within the BI and surrounding tissue, after 4, 14, and 28 days of implantation are shown in Fig. 4b, d. The process displays that there is no infiltration of macrophages, with no significant changes observed in the color intensities. In Fig. 4b, the reduction in the spread of the red fluorescence with time emphasizes the nonappearance of inflammation, with the CD68 expected to stain the macrophages red.

Explanted samples were inspected to analyze the significant host tissue infiltration within the implanted sample. While the short length of the study precluded complete scaffold

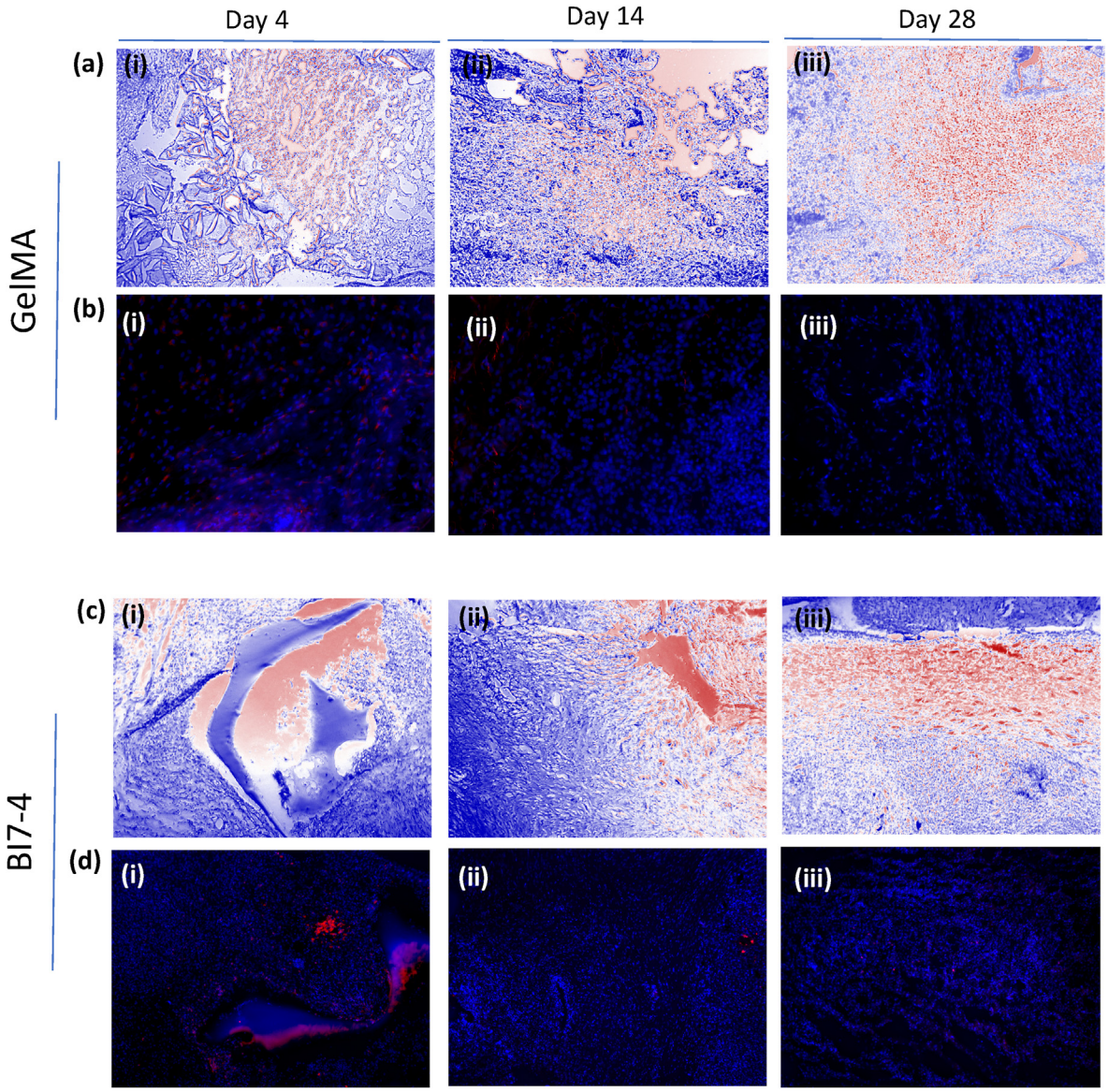

Fig. 4. *In vivo* biocompatibility of GelMA and BI7-4. Representative **(a, c)** H&E staining, **(b, d)** fluorescent immunohistochemical analysis of macrophage marker (CD68) of bio-ionic ink explanted with surrounding tissue after (i) 4, (ii) 14, and (iii) 28 days of implantation, counterstained with DAPI.

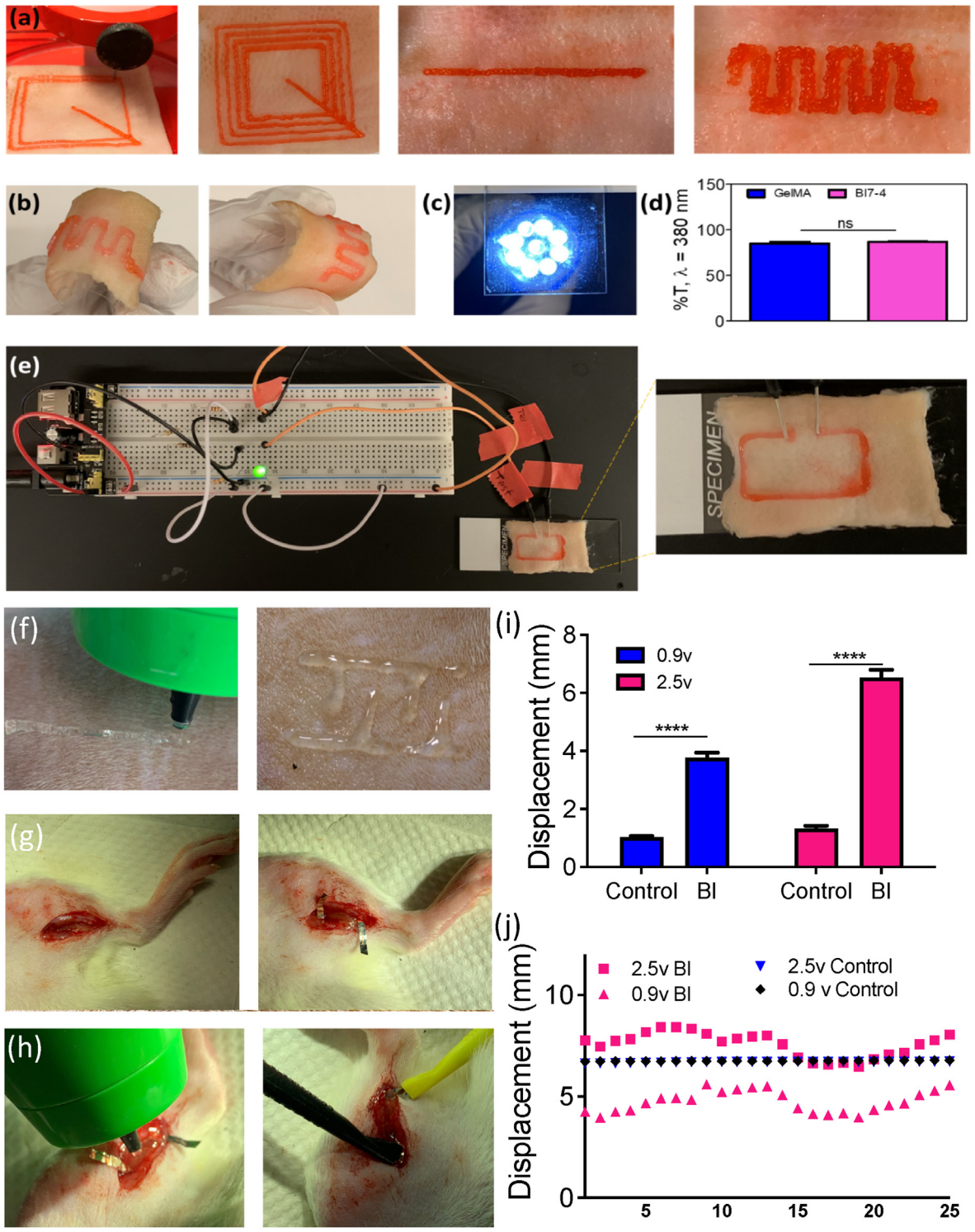

Fig. 5. 3D printing of BI7-4 on porcine skin **(a)** Digital image of printing bio-ionic ink (BI) using Allevi 2 printer in different shapes. **(b)** Digital image showing the adherence and bending of the printed ink on the skin. **(c)** Transparency of the BI coated on microscope slide illuminated using a flashlight. **(d)** Transparency (%T) of 7% GelMA, and BI7-4, calculated from the absorbance at a wavelength of 380 nm using a spectrophotometer. **(e)** Digital image to show the printed BI7-4 illuminating the LED of a 1 V power source. *In vivo* electrical stimulation of TA muscle and 3D printing of BI, representing digital images of **(f)** 3D printing of BI on the back of Wistar rat, indicating various shapes. **(g, h)** An incision in the hind muscle, incorporation of standard platinum electrodes with 10 mm separation, 3D printing of BI in the 5 mm separation space, inducing voltage across the electrodes. **(i, j)** Quantification of the displacement of TA muscle during electrical stimulation at two different voltages, 0.9 V, and 2.5 V, along with the displacement of muscle without the BI and only Pt electrode (control) and with the BI. P values were determined by one-way ANOVA (*P < 0.05, **P < 0.01, ****P < 0.001), ns – non-significant.

biodegradation, previous works have demonstrated that GelMA-based hydrogels facilitate cell-mediated degradation *in vivo* [16,19], indicating that the degradation of the BI *in vivo,* can be a parameter that can be adjusted based on the application. The BIL-conjugated GelMA, upon administration *in vivo,* may be thought of as interacting with blood components like the erythrocytes and plasma proteins resulting in aggregation or dissociation. Additionally, the aforementioned interactions with cell membranes, extracellular matrix, and proteins lead to adverse effects [62].

3.7. Ex vivo and in vivo 3D printing of the bio-ionic ink and evaluation of conductivity

To study the printability and shape fidelity of the BI, we performed *ex vivo* and *in vivo* studies. For the ideal implementation of a bio-ink as an interface between biological systems and electronics, it must exhibit superior performance without undergoing any significant deformation during the printing process. Fig. 5 shows the 3D printing of different shapes of BI7-4 on the epidermal layer of the porcine skin showing the ability of the BI to adhere to the tissue. Fig. S4 exhibits the 3D printing of BI7-4 on porcine skin and shows the printed BI7-4 illuminating the LED at various voltages of 2, 3, 4, and 5 V. Fig. 5a shows the digital image of printing BI using an Allevi 2 printer in different shapes. In Fig. 5b the polymerized BI7-4 construct is shown to be firmly attached to the skin substantiating the adhesive property of the ink. Transparency of the BI coated on a microscope slide illuminated using a flashlight is shown in Fig. 5c indicating no significant changes in the transparency of the ink due to the addition of the BIL compared to GelMA in Fig. 2h. To verify the conductive property of BI, the printed BI7-4 was connected to the breadboard setup with an input voltage of 5 V, which when connected to the specimen acts as a circuit and thus illuminating the LED of a 1 V power source. Fig. S3 shows the LED at various voltages. Finally, a successful demonstration of 3D printing of a conductive and adhesive BI was attainable.

Skeletal muscle tissue stimulation experiments were performed to underscore that BioGel hydrogel successfully interfaces with soft tissues in an *in vivo* electrical stimulation experiment. Fig. 5f–h indicates the ability of the BI to be used as conductive ink for actuation via *in vivo* electrical stimulation of TA muscle and *in situ* 3D printing of different shapes of BI7-4 on the rat skin, showing the ability of the BI to integrate with the tissue. In addition, the *in vivo* electrical stimulation experiment was conducted to investigate the ability of the bio-ink to integrate and be used as an interface with soft tissue. Platinum (Pt) electrodes were used, and the TA muscle was exposed surgically after fixing the knee of the Wistar rat for electrical stimulation. The BI was then printed on the exposed muscle across the Pt electrode. The TA muscle was electrically stimulated at 0.9 and 2.5 V to measure twitch displacement. The contraction of the TA muscle was significantly higher when the electrode interface was connected by 3D printed BI compared to the control; the displacement increased from 3.95 mm at a stimulation voltage of 0.9 V–6.5 mm with stimulation voltages of 2.5 V (Fig. 5i and j). These data denote that the conductivity of the BI can be harnessed and manipulated according to the application, which may be beneficial in a clinical application where conductive hydrogels are desired. Also, we were able to demonstrate the bio-ink's ability to print on the skin, and it is important to note that the BI can be used as an innovative material for flexible electronics due to its tunable functionalities and versatile design. These data suggest that the BI can be a potential solution for the current challenges and limitations of *in situ* 3D printing of bioelectronics at the interface of biological tissue.

Thus, BioGel bio-ink uniquely allowed for the in-situ formation of stable ionic circuits fully compatible with biological systems - significant progress for the field of wearable electronics and bioelectronics. This BioGel hydrogel bio-ink offers new possibilities for biologically paired electronic systems, creating seamless interfaces with living tissues to produce conductive signals with decreased tissue injury and minimum interfacial transformation losses. As a result, BIL-functionalized hydrogels can be usefully applied in ionic-electronic interface systems for sensors and actuator applications. Additionally, the biocompatibility of such systems encourages their possibility as a soft, multifunctional biomaterial in biological applications.

4. Conclusion

Here, we report synthesizing a novel in-situ 3D printable BI composed of acrylated BIL conjugated using visible light photocrosslinking. The synthesis establishes a general material platform that can be applied to a wide variety of biopolymers and BIL to obtain printable bio-inks with a wide variety of biomimetic properties that can aid in cell growth as well as act as an electroconductive tissue scaffold. We demonstrated that the BI's physiomechanical properties and electrical conductivity could be enhanced and tailored to suit the requirements of biomedical and bioelectronic applications by varying the BIL content in the biohydrogel backbone. The printability of the resultant biomaterials was shown by rheological analysis and structural details in printed constructs. The composite bio-ink was processed into multilayer scaffolds via 3D printing and visible light crosslinking. Furthermore, cell growth and viability tests demonstrate virtuous biocompatibility of the bio-ink allowing cell proliferation. Functionalization of the biopolymer backbone with the BIL was also shown to improve cellular adhesion and reduce potential fouling. The versatility of the polymer backbone chemistry, its processing conditions as well as the type and content of BIL functionalization offer a generalized platform for the production of biomaterial for easy, rapid in-situ 3D bioprinting of complex designs directly on biological tissue. Furthermore, the BioGel bio-ink provides versatile compositions for bioelectronics fabrication while avoiding tissue injury from electrical stimulation.

Author contributions

Iman Noshadi, Vaishali Krishnadoss: Conceptualization, Methodology. **Iman Noshadi, Baishali Kanjilal:** Writing - original draft, review & editing. **Vaishali Krishnadoss:** Data curation. **Arameh Masoumi, Aihik Banerjee, Iman Dehzangi, Jeroen Leijten, Arash Pezhouman, Reza Ardehali, Manuela Martins-Green:** Validation, Writing – review & editing. **Iman Noshadi:** Supervision, Project administration, Funding acquisition.

Funding sources

The authors are grateful for financial support from the UC RiversideStartupFund and NSF 1919092 and 2136603 awards and CIRM-TRANSCEND (Award#:EDUC4-12752).

The raw/processed data required to reproduce these findings cannot be shared at this time due to technical or time limitations.

Declaration of competing interest

The authors declare that they have no known competing financial interests or personal relationships that could have appeared to influence the work reported in this paper.

Data availability

Data will be made available on request.

Appendix A. Supplementary data

Supplementary data to this article can be found online at https://doi.org/10.1016/j.mtadv.2023.100352.

References

[1] S.V. Murphy, A. Atala, 3D bioprinting of tissues and organs, Nat. Biotechnol. 32 (2014) 773–785, https://doi.org/10.1038/nbt.2958.

[2] S.H. Jariwala, G.S. Lewis, Z.J. Bushman, J.H. Adair, H.J. Donahue, 3D printing of personalized artificial bone scaffolds, 3D Print. Addit. Manuf. 2 (2015) 56–64, https://doi.org/10.1089/3dp.2015.0001.

[3] T.G. Papaioannou, D. Manolesou, E. Dimakakos, G. Tsoucalas, M. Vavuranakis, D. Tousoulis, 3D bioprinting methods and techniques: applications on artificial blood vessel fabrication, Acta Cardiol. Sin. 35 (2019) 284–289, https://doi.org/10.6515/ACS.201905_35(3).20181115A.

[4] D. Min, W. Lee, I.-H. Bae, T.R. Lee, P. Croce, S.-S. Yoo, Bioprinting of biomimetic skin containing melanocytes, Exp. Dermatol. 27 (2018) 453–459, https://doi.org/10.1111/exd.13376.

[5] C.L. Ventola, Medical applications for 3D printing: current and projected uses, P T 39 (2014) 704–711. PMID: 25336867.

[6] B.V. Slaughter, S.S. Khurshid, O.Z. Fisher, A. Khademhosseini, N.A. Peppas, Hydrogels in regenerative medicine, Adv. Mater. 21 (2009) 3307–3329, https://doi.org/10.1002/adma.200802106.

[7] A.S. Hoffman, Hydrogels for biomedical applications, Adv. Drug Deliv. Rev. 64 (2012) 18–23, https://doi.org/10.1016/j.addr.2012.09.010.

[8] I. Donderwinkel, J.C.M. van Hest, N.R. Cameron, Bio-inks for 3D bioprinting: recent advances and future prospects, Polym. Chem. 8 (2017) 4451–4471, https://doi.org/10.1039/C7PY00826K.

[9] M.P. Nikolova, M.S. Chavali, Recent advances in biomaterials for 3D scaffolds: a review, Bioact. Mater. 4 (2019) 271–292, https://doi.org/10.1016/j.bioactmat.2019.10.005.

[10] A. Saberi, F. Jabbari, P. Zarrintaj, M.R. Saeb, M. Mozafari, Electrically conductive materials: opportunities and challenges in tissue engineering, Biomolecules 9 (2019) 1–56, https://doi.org/10.3390/biom9090448.

[11] R. Balint, N.J. Cassidy, S.H. Cartmell, Conductive polymers: towards a smart biomaterial for tissue engineering, Acta Biomater. 10 (2014) 2341–2353, https://doi.org/10.1016/j.actbio.2014.02.015.

[12] S.R. Shin, et al., Carbon nanotube reinforced hybrid microgels as scaffold materials for cell encapsulation, ACS Nano 6 (2012) 362–372, https://doi.org/10.1021/nn203711s.

[13] S.R. Shin, et al., Carbon-nanotube-embedded hydrogel sheets for engineering cardiac constructs and bioactuators, ACS Nano 7 (2013) 2369–2380, https://doi.org/10.1021/nn305559j.

[14] J.H. Min, M. Patel, W.-G. Koh, Incorporation of conductive materials into hydrogels for tissue engineering applications, Polymers 10 (2018) 1–36, https://doi.org/10.3390/polym10101078.

[15] Y. Zhang, et al., Cytotoxicity effects of graphene and single-wall carbon nanotubes in neural phaeochromocytoma-derived PC12 cells, ACS Nano 4 (2010) 3181–3186, https://doi.org/10.1021/nn1007176.

[16] V. Krishnadoss, et al., Bioionic liquid conjugation as universal approach to engineer hemostatic bioadhesives, ACS Appl. Mater. Interfaces 11 (2019) 38373–38384, https://doi.org/10.1021/acsami.9b08757.

[17] B.W. Walker, et al., Engineering a naturally-derived adhesive and conductive cardiopatch, Biomaterials 207 (2019) 89–101, https://doi.org/10.1016/j.biomaterials.2019.03.015.

[18] R. Vijayaraghavan, et al., Biocompatibility of choline salts as crosslinking agents for collagen based biomaterials, Chem. Commun. 46 (2010) 294–296, https://doi.org/10.1039/B910601D.

[19] I. Noshadi, et al., Engineering biodegradable and biocompatible bio-ionic liquid conjugated hydrogels with tunable conductivity and mechanical properties, Sci. Rep. 7 (2017) 1–18, https://doi.org/10.1038/s41598-017-04280-w.

[20] B.D. Fairbanks, M.P. Schwartz, C.N. Bowman, K.S. Anseth, Photoinitiated polymerization of PEG-diacrylate with lithium phenyl-2,4,6-trimethylbenzoylphosphinate: polymerization rate and cytocompatibility, Biomaterials 30 (2009) 6702–6707, https://doi.org/10.1016/j.biomaterials.2009.08.055.

[21] L. Ge, S. Chen, Recent advances in tissue adhesives for clinical medicine, Polymers 12 (2020) 1–22, https://doi.org/10.3390/polym12040939.

[22] A. Assmann, et al., A highly adhesive and naturally derived sealant, Biomaterials 140 (2017) 115–127, https://doi.org/10.1016/j.biomaterials.2017.06.004.

[23] G.M. Taboada, et al., Overcoming the translational barriers of tissue adhesives, Nat. Rev. Mater. 5 (2020) 310–329, https://doi.org/10.1038/s41578-019-0171-7.

[24] S. Lee, E.S. Sani, A.R. Spencer, Y. Guan, A.S. Weiss, N. Annabi, Human-recombinant-elastin-based bioinks for 3D bioprinting of vascularized soft tissues, Adv. Mater. 32 (2020) 1–10, https://doi.org/10.1002/adma.202003915.

[25] S. Zhao, et al., Programmable hydrogel ionic circuits for biologically matched electronic interfaces, Adv. Mater. 30 (2018) 1–10, https://doi.org/10.1002/adma.201800598.

[26] C. Mandrycky, K. Phong, Y. Zheng, Tissue engineering toward organ-specific regeneration and disease modeling, MRS Commun 7 (2017) 332–347, https://doi.org/10.1557/mrc.2017.58.

[27] K. Kimura, J. Motomatsu, Y. Tominaga, Correlation between solvation structure and ion-conductive behavior of concentrated poly(ethylene carbonate)-based electrolytes, J. Phys. Chem. C 120 (2016) 12385–12391, https://doi.org/10.1021/acs.jpcc.6b03277.

[28] J. Ding, et al., Electrospun polymer biomaterials, Prog. Polym. Sci. 90 (2019) 1–34, https://doi.org/10.1016/j.progpolymsci.2019.01.002.

[29] X. Yu, et al., Polyvalent choline phosphate as a universal biomembrane adhesive, Nat. Mater. 11 (2012) 468–476, https://doi.org/10.1038/nmat3272.

[30] J. Li, et al., Tough adhesives for diverse wet surfaces, Science 357 (2017) 378–381, https://doi.org/10.1126/science.aah6362.

[31] L. Han, et al., Tough, self-healable and tissue-adhesive hydrogel with tunable multifunctionality, NPG Asia Mater. 9 (2017) 1–12, https://doi.org/10.1038/am.2017.33.

[32] A. Sacco, Electrochemical impedance spectroscopy: fundamentals and application in dye-sensitized solar cells, Renew. Sustain. Energy Rev. 79 (2017) 814–829, https://doi.org/10.1016/j.rser.2017.05.159.

[33] S.B. Aziz, T.J. Woo, M.F.Z. Kadir, H.M. Ahmed, A conceptual review on polymer electrolytes and ion transport models, J. Sci.: Adv. Mat. Devices 3 (2018) 1–17, https://doi.org/10.1016/j.jsamd.2018.01.002.

[34] M. Coşkun, Ö. Polat, F.M. Coşkun, Z. Durmuş, M. Çağlar, A. Türüt, The electrical modulus and other dielectric properties by the impedance spectroscopy of LaCrO3 and LaCr0.90Ir0.10O3 perovskites, RSC Adv. 8 (2018) 4634–4648, https://doi.org/10.1039/C7RA13261A.

[35] D. Qu, H. Shi, Studies of activated carbons used in double-layer capacitors, J. Power Sources 74 (1998) 99–107, https://doi.org/10.1016/S0378-7753(98)00038-X.

[36] F. Ganji, S. Vasheghani Farahani, E. Vasheghani-Farahani, Theoretical description of hydrogel swelling: a review, Iran. Polym. J. (Engl. Ed.) 19 (2010) 375–398.

[37] P.M. Kharkar, K.L. Kiick, A.M. Kloxin, Designing degradable hydrogels for orthogonal control of cell microenvironments, Chem. Soc. Rev. 42 (2013) 7335–7372, https://doi.org/10.1039/C3CS60040H.

[38] C.M. Runnels, et al., Folding, assembly, and persistence: the essential nature and origins of biopolymers, J. Mol. Evol. 86 (2018) 598–610, https://doi.org/10.1007/s00239-018-9876-2.

[39] D.M. Lynn, R. Langer, Degradable poly(β-amino esters): synthesis, characterization, and self-assembly with plasmid DNA, J. Am. Chem. Soc. 122 (2000) 10761–10768, https://doi.org/10.1021/ja0015388.

[40] D. Fischer, Y. Li, B. Ahlemeyer, J. Krieglstein, T. Kissel, In vitro cytotoxicity testing of polycations: influence of polymer structure on cell viability and hemolysis, Biomaterials 24 (2003) 1121–1131, https://doi.org/10.1016/s0142-9612(02)00445-3.

[41] G. Grandinetti, N.P. Ingle, T.M. Reineke, Interaction of poly(ethylenimine)–DNA polyplexes with mitochondria: implications for a mechanism of cytotoxicity, Mol. Pharm. 8 (2011) 1709–1719, https://doi.org/10.1021/mp200078n.

[42] P.R. Leroueil, et al., Wide varieties of cationic nanoparticles induce defects in supported lipid bilayers, Nano Lett. 8 (2008) 420–424, https://doi.org/10.1021/nl0722929.

[43] S. Vaidyanathan, B.G. Orr, M.M. Banaszak Holl, Role of cell membrane–vector interactions in successful gene delivery, Accounts Chem. Res. 49 (2016) 1486–1493, https://doi.org/10.1021/acs.accounts.6b00200.

[44] A.M. Seddon, D. Casey, R.V. Law, A. Gee, R.H. Templer, O. Ces, Drug interactions with lipid membranes, Chem. Soc. Rev. 38 (2009) 2509–2519, https://doi.org/10.1039/B813853M.

[45] B.D. Monnery, et al., Cytotoxicity of polycations: relationship of molecular weight and the hydrolytic theory of the mechanism of toxicity, Int. J. Pharm. 521 (2017) 249–258, https://doi.org/10.1016/j.ijpharm.2017.02.048.

[46] D. Sgouras, R. Duncan, Methods for the evaluation of biocompatibility of soluble synthetic polymers which have potential for biomedical use: 1 — use of the tetrazolium-based colorimetric assay (MTT) as a preliminary screen for evaluation of in vitro cytotoxicity, J. Mater. Sci. Mater. Med. 1 (1990) 61–68, https://doi.org/10.1007/bf00839070.

[47] D. Zhong, et al., Effects of the gene carrier polyethyleneimines on structure and function of blood components, Biomaterials 34 (2013) 294–305, https://doi.org/10.1016/j.biomaterials.2012.09.060.

[48] A.C. Hunter, Molecular hurdles in polyfectin design and mechanistic background to polycation induced cytotoxicity, Adv. Drug Deliv. Rev. 58 (2006) 1523–1531, https://doi.org/10.1016/j.addr.2006.09.008.

[49] P. Chollet, M.C. Favrot, A. Hurbin, J.-L. Coll, Side-effects of a systemic injection of linear polyethylenimine–DNA complexes, J. Gene Med. 4 (2002) 84–91, https://doi.org/10.1002/jgm.237.

[50] K. Kim, W.C.W. Chen, Y. Heo, Y. Wang, Polycations and their biomedical applications, Prog. Polym. Sci. 60 (2016) 18–50, https://doi.org/10.1016/j.progpolymsci.2016.05.004.

[51] D.M. Morgan, J. Clover, J.D. Pearson, Effects of synthetic polycations on leucine

incorporation, lactate dehydrogenase release, and morphology of human umbilical vein endothelial cells, J. Cell Sci. 91 (1988) 231–238, https://doi.org/10.1242/jcs.91.2.231.
[52] D.M. Morgan, V.L. Larvin, J.D. Pearson, Biochemical characterisation of polycation-induced cytotoxicity to human vascular endothelial cells, J. Cell Sci. 94 (1989) 553–559, https://doi.org/10.1242/jcs.94.3.553.
[53] C.C.A. Ng, et al., Using an electrical potential to reversibly switch surfaces between two states for dynamically controlling cell adhesion, Angew. Chem. Int. Ed. 51 (2012) 7706–7710, https://doi.org/10.1002/anie.201202118.
[54] B.M. Lamb, M.N. Yousaf, Redox-switchable surface for controlling peptide structure, J. Am. Chem. Soc. 133 (2011) 8870–8873, https://doi.org/10.1021/ja203198y.
[55] C. Saltó, et al., Control of neural stem cell adhesion and density by an electronic polymer surface switch, Langmuir 24 (2008) 14133–14138, https://doi.org/10.1021/la8028337.
[56] A.A. Khalili, M.R. Ahmad, A review of cell adhesion studies for biomedical and biological applications, Int. J. Mol. Sci. 16 (2015) 18149–18184, https://doi.org/10.3390/ijms160818149.
[57] G. Fuhr, P.I. Kuzmin, Behavior of cells in rotating electric fields with account to surface charges and cell structures, Biophys. J. 50 (1986) 789–795, https://doi.org/10.1016/S0006-3495(86)83519-6.
[58] W.J. Choi, et al., Effects of substrate conductivity on cell morphogenesis and proliferation using tailored, atomic layer deposition-grown ZnO thin films, Sci. Rep. 5 (2015) 1–9, https://doi.org/10.1038/srep09974.
[59] T. Gao, et al., Optimization of gelatin-alginate composite bioink printability using rheological parameters: a systematic approach, Biofabrication 10 (2018), 034106, https://doi.org/10.1088/1758-5090/aacdc7.
[60] D. Chimene, K.K. Lennox, R.R. Kaunas, A.K. Gaharwar, Advanced bioinks for 3D printing: a materials science perspective, Ann. Biomed. Eng. 44 (2016) 2090–2102, https://doi.org/10.1007/s10439-016-1638-y.
[61] H. Yuk, B. Lu, X. Zhao, Hydrogel bioelectronics, Chem. Soc. Rev. 48 (2019) 1642–1667, https://doi.org/10.1039/C8CS00595H.
[62] R. Kircheis, L. Wightman, E. Wagner, Design and gene delivery activity of modified polyethylenimines, Adv. Drug Deliv. Rev. 53 (2001) 341–358, https://doi.org/10.1016/s0169-409x(01)00202-2.
[63] E.S. Place, J.H. George, C.K. Williams, M.M. Stevens, Synthetic polymer scaffolds for tissue engineering, Chem. Soc. Rev. 38 (2009) 1139–1151, https://doi.org/10.1039/B811392K.
[64] S. Sahoo, J.G. Cho-Hong, T. Siew-Lok, Development of hybrid polymer scaffolds for potential applications in ligament and tendon tissue engineering, Biomed. Mater. 2 (2007) 169–173, https://doi.org/10.1088/1748-6041/2/3/001.
[65] R. Langer, J. Vacanti, Tissue engineering, Science 260 (1993) 920–926, https://doi.org/10.1126/science.8493529.
[66] A.S. Rowlands, S.A. Lim, D. Martin, J.J. Cooper-White, Polyurethane/poly(lactic-co-glycolic) acid composite scaffolds fabricated by thermally induced phase separation, Biomaterials 28 (2007) 2109–2121, https://doi.org/10.1016/j.biomaterials.2006.12.032.
[67] S. Huang, C. Wang, J. Xu, L. Ma, C. Gao, In situ assembly of fibrinogen/hyaluronic acid hydrogel via knob-hole interaction for 3D cellular engineering, Bioact. Mater. 2 (2017) 253–259, https://doi.org/10.1016/j.bioactmat.2017.09.002.
[68] M. Hussain, J. Wackerlig, P.A. Lieberzeit, Biomimetic strategies for sensing biological species, Biosensors 3 (2013) 89–107, https://doi.org/10.3390/bios3010089.
[69] X.-D. Hou, Q.-P. Liu, T.J. Smith, N. Li, M.-H. Zong, Evaluation of toxicity and biodegradability of cholinium amino acids ionic liquids, PLoS One 8 (2013) 1–7, https://doi.org/10.1371/journal.pone.0059145.
[70] L.M. Sanders, S. H. Choline Zeisel, Dietary requirements and role in brain development, Nutr. Today 42 (2007) 181–186, https://doi.org/10.1097/01.NT.0000286155.55343.